Confined Diffusion in Periodic Porous Nanostructures

Riccardo Raccis,[†] Arash Nikoubashman,[‡] Markus Retsch,[†] Ulrich Jonas,[§] Kaloian Koynov,[†] Hans-Jürgen Butt,[†] Christos N. Likos,[⊥] and George Fytas[†,∥,¶,*]

[†]Max Planck Institute for Polymer Research, Ackermannweg 10, 55128 Mainz, Germany, [‡]Institute of Theoretical Physics and CMS, Vienna University of Technology, Wiedner Hauptstrasse 8-10, A-1040 Vienna, Austria, [§]Bio-Organic Materials Chemistry Laboratory (BOMCLab), Institute of Electronic Structure and Laser, FORTH, 71110 Heraklion, Greece, [⊥]Faculty of Physics, University of Vienna, Boltzmanngasse 5, A-1090 Vienna, Austria, [∥]Institute of Electronic Structure and Laser, FORTH, 71110 Heraklion, Greece, and [¶]Department of Materials Science, University of Crete, 71110 Heraklion, Greece

Mass transport has attracted strong interest since the first observation of Brownian motion in the eighteenth century. Diffusion is ubiquitous in nature and is at work in many processes and applications including biorelated fields,[1,2] energy conversion and storage (fuel and solar cells),[3] separation membranes,[4] and microfluidics.[5,6] With increasing complexity of such novel devices involving hierarchically structured materials, it becomes evident that mass and analyte transport have to be understood on a variety of time and length scales. Alongside the elucidation of the diffusion law[7−9] comes the increase in interface and geometrical constraints of the motion.[10] Constrained macromolecular diffusion underlies many separation methods,[11,12] plays an important role in intracellular and extracellular transport,[13] and, in addition, has important ramifications of fundamental scientific interest.[14] Therefore, extensive research across different disciplines[13,15] and diverse materials[8,9,16] was devoted to establishing diffusion laws and relationships to geometrical and topological characteristics of the diffusing species and medium.

The advent of powerful experimental techniques allowing single-molecule detection, the fabrication of patterned nanostructures with built-in spatial constraints, and the development of computational tools conveyed the exploration of diffusion dynamics in complex environments.[5,7,8,17,18] The earlier experiments[6,10] on large DNA molecules for direct visualization indicate that switching from disordered to patterned media holds promise for a better understanding of the diffusion fundamentals and improved performance of devices for the different applications. The strategy of patterned system utilization to obstruct diffusion has been implemented through microfabrication of fluidic devices[5,6]

ABSTRACT We performed fluorescence correlation spectroscopy measurements to assess the long-time self-diffusion of a variety of spherical tracer particles in periodic porous nanostructures. Inverse opal structures with variable cavity sizes and openings in the nanometer domain were employed as the model system. We obtained both the exponent of the scaling relation between mean-square displacement and time and the slow-down factors due to the periodic confinement for a number of particle sizes and confining characteristics. In addition, we carried out Brownian dynamics simulations to model the experimental conditions. Good agreement between experimental and simulation results has been obtained regarding the slow-down factor. Fickian diffusion is predicted and seen in almost all experimental systems, while apparent non-Fickian exponents that show up for two strongly confined systems are attributed to polydispersity of the cavity openings. The utility of confining periodic porous nanostructures holds promise toward understanding of constrained diffusion with a wide range of applications ranging from water purification and drug delivery to tissue engineering.

KEYWORDS: periodic structures · confined diffusion · Brownian dynamics simulation · fluorescence correlation spectroscopy

and colloidal templates,[10] respectively, for size-dependent trapping and diffusion through molecular size obstructions. Extension to nanoporous systems was exemplified in surfactant-templated mesoporous silica for diffusion and interaction-controlled mass transport[16] and drug delivery.[2,18] However, unique assignment of the role of geometrical and topological characteristics of periodic nanostructures on the basic diffusion mechanisms is better performed on simple rigid probes rather than long biopolymers with configurational freedom and complex interactions with the walls of the patterned media.

In this paper, we report on the tracer diffusion of spherical quantum dot particles (abbreviated as QDs) confined in a three-dimensional inverse opal with well-defined highly ordered structure and different geometrical constraints using the single-molecule technique of fluorescence correlation spectroscopy (FCS).[16,19−22] This technique has been recently utilized to probe

one-dimensional diffusion of molecular and macromolecular tracers in nanoporous alumina membranes[23,24] and three-dimensional diffusion of molecular tracers in silica inverse opals.[25] The former has simply shown the feasibility of the technique to measure the retarded mobility inside the nanopores, while the very recent study in large void opals reported on complex non-Fickian diffusion. We found that the QD particles undergo a single Fickian diffusion, and the long-time self-diffusion coefficient D is slowed down with increasing ratio of the particle radius a to the opal cavity radius R at a constant opening hole diameter L. Brownian dynamics simulation using a Yukawa-like interaction potential between particle and cavity wall quantitatively captures the slowing down as well as the limiting value of D in the limit $(a/R) \rightarrow 0$.

On the basis of these findings, we expect new material and nanostructure designs to emerge, as well as a better understanding of existing devices to be gained. The slow-down factor paradigm is scalable and hence can be applied to a wide range of nanostructured materials. For instance, increase in interface and constrained diffusion can help to design compartments of intrinsically long reaction/detection times. Emerging filters and membranes[4] increasingly push for high surface areas to interact more effectively with any type of analytes. The large interface model system studied here adds to our knowledge toward targeting of these needs.

RESULTS AND DISCUSSION

Confined Tracer Diffusion. We fabricated three different inverse colloidal crystals (i-opals). Table 1 summarizes the characteristic dimensions, cavity radius R and hole diameter L, obtained from the SEM images (see Figure 8 in the Methods section) of the i-opals along with their thickness d.

The three systems are characterized by different constraining geometries, expressed in the ratio L/R whose values can be varied by changing either the hole diameter at constant void radius (in the case of iO180-12/15 and iO180-10/15) or both in the case of the iO130-9/11 membrane. The diffusion of several fluorescent probes (see Table 3 in the Methods section) in the HEPES (Sigma-Aldrich, pH 7.4, concentration 0.01 M) filled inverse opals was studied by FCS. The method is based on measurement of the fluctuations of the fluorescent light intensity caused by the excursion of fluorescent probes through an extremely small observation volume (<1 μm^3) defined by the focus of a confocal microscope (see Methods). In the FCS experiment, the fluorescent probes were excited by two different lasers, $\lambda = 633$ nm for T1.3 and $\lambda = 488$ nm for QDs (see Methods), leading to slightly different probed volumes, as illustrated in Figure 1. As it has been shown theoretically for an ensemble of identical, freely diffusing fluorescent species, the FCS autocorrelation function $G(t)$ (see Methods) has the following

TABLE 1. Geometrical Characteristic Dimensions (Cavity Radius R, Hole Diameter L) for the Inverse Opals with Thickness d

| samples/sizes	iO180-12/15	iO180-10/15	iO130-9/11
thickness d (μm)	7.4	4.6	5.0
R (nm)	75	75	55
L (nm)	60	50	45
L/R	12/15	10/15	9/11
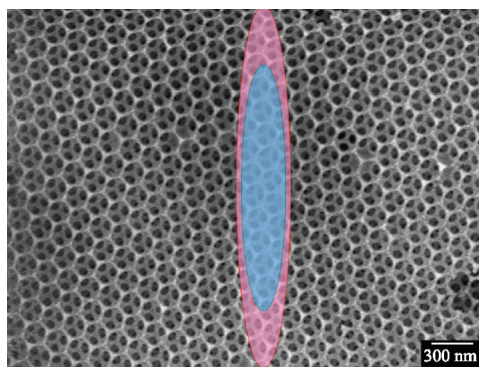
Figure 1. Scanning electron microscopy (SEM) image of the inverse opal (iO180-12/15) (see Table 1) along with the observation volumes in the FCS experiment for excitation at the wavelength $\lambda = 488$ nm (azure) and $\lambda = 633$ nm (pink), respectively, for QD and T1.3.

analytical form:[19,20]

$$G(t) = 1 + \frac{1}{N} \frac{1}{\left(1 + \frac{t}{\tau}\right)\sqrt{1 + \frac{t}{\tau S^2}}} \quad (1)$$

Here, $N = 1/[G(t = 0) - 1]$ is the average number of species in the observation volume, $S = z_0/r_0$ is the ratio between longitudinal and transversal dimensions of the observation volume, and τ is the diffusion time of the species, which is related to their diffusion coefficient, D, through $\tau = r_0^2/4D$. Equation 1 is derived assuming that the fluorescence properties of the diffusing species do not change while they pass through the observation volume. However, this assumption is often not true because various photophysical effects may lead to additional fluctuations in the fluorescence intensity. Two types of photophysical effects were applied in our study. For the molecular probe T1.3 (Table 3), the dominating effect was the transition of the molecule to the first excited triplet state. While staying at this rather long-living state, the molecule appeared dark, an effect that led to fluctuations of the fluorescent intensity, typically at the microsecond time scale. This resulted in an additional exponential decay in the autocorrelation function $G(t)$, which modifies to[19,20]

$$G(t) = 1 + \left[1 + \frac{f_T}{1 - f_T}\exp(-t/\tau_T)\right]\frac{1}{N}\frac{1}{\left(1 + \frac{t}{\tau}\right)\sqrt{1 + \frac{t}{\tau S^2}}} \quad (2)$$
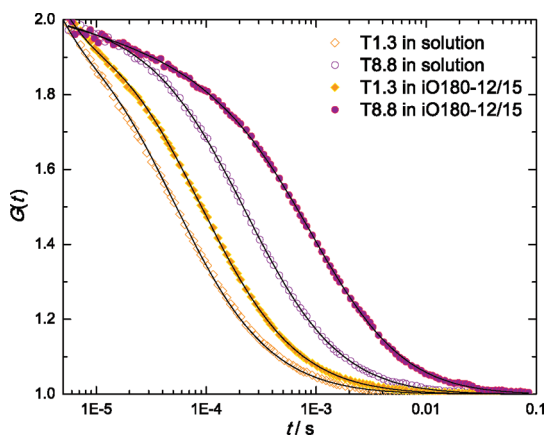
Figure 2. Experimental autocorrelation functions $G(t)$ for the diffusion of the molecular T1.3 and QD T8.8 tracer in a (iO180-12/15) i-opal and in the free aqueous solution. Continuous lines denote the representation of $G(t)$ by either eq 2 (for the molecular tracer) or eq 3 (for the QD), as indicated by the shift of the corresponding $G(t)$ and the description in the plot.

where f_T and τ_T are the fraction and the decay time of the triplet state. Typically, τ_T is in the order of a few microseconds. Equation 2 leads to an excellent representation of the experimental $G(t)$ for T1.3 diffusing either in free aqueous solution or in the i-opals, as seen (solid lines) in Figure 2.

In the case of QDs, the photophysical effects were different. Instead of triplet kinetics, they exhibited an on−off emission (blinking) with dark times ranging from nanoseconds to seconds.[26] The blinking fluctuations are represented by a power-law time dependence, and eq 1 is now written as[26,27]

$$G(t) = 1 + A(1 - Bt^{2-m})\frac{1}{N}\frac{1}{\left(1+\dfrac{t}{\tau}\right)\sqrt{1+\dfrac{t}{\tau S^2}}} \quad (3)$$

where A describes the overall amplitude of the blinking effect and B the strength of the power law dependence with the characteristic exponent m. Since $N = A/[G(0) - 1]$ should be invariant of the intrinsic contribution, $A = 1$. Further, since the blinking parameters depend[26] on the QDs' structure, environment, excitation intensity, and observation time, both $B > 0$ and m have to be treated as floating parameters in the fitting procedure of eq 3 to the experimental $G(t)$. As seen in Figure 2, the latter is very well described by eq 3, yielding $m \approx 1.8$, which is in a good agreement with previously reported values.[26,27]

The restricted environment exerted a clear slow-down effect on the center of mass motion for both T1.3 and QDs as shown by the experimental $G(t)$ in the i-opal (with $L/R = 12/15$) and in the free solution in Figure 2. Prior to the discussion of this pertinent finding, it should be stressed that differences in the imaging conditions in the pure water and water-filled i-opal media do not affect the reported slow-down

effect. In our experiment, the objective's immersion medium was water with refractive index $n \approx 1.33$. For the water-filled i-opal with a silica ($n \approx 1.45$) filling volume fraction of about 25%, the effective refractive index was $n \approx 1.36$. Due to this small n mismatch, the estimated error of the diffusion in the i-opals was less than 10%.[28,29] Thus the strong shift of the autocorrelation curves for the i-opals toward to longer times (Figure 2) was caused by the confinement, as discussed and theoretically rationalized below.

Modeling and Simulation. We employed a standard Brownian dynamics (BD) simulation approach in order to simulate the diffusive behavior of a small spherical particle (radius a), which is embedded into an inverse opal with cavity radius R and opening diameter L. The angle of aperture is then defined as $\vartheta_0 = \arcsin(L/2\pi)$ and the distance of the opening as $h = [(R^2 - L^2)/4]^{1/2}$. For better comprehension, we provide a schematic representation of such a system in Figure 3.

Since the Reynolds number, Re, of such a colloidal system is very small (Re $\ll$ 1), the movement of the particle can be considered as overdamped, and hence the equation of motion reduces to a stochastic position process:

$$\mathbf{r}(t + \Delta t) = \mathbf{r}(t) + \Delta t \frac{D_S}{k_B T}\mathbf{F}(r) + \mathbf{r}_G \quad (4)$$

Here, D_S denotes the short-time diffusion coefficient, k_B is Boltzmann's constant, and $\mathbf{F}(r)$ is the deterministic force exerted by the confining cavity, arising from the wall-particle potential $U(r)$ as $\mathbf{F}(r) = -\nabla U(r)$. The vector $\mathbf{r}_G$ is a random variable drawn from a Gaussian distribution with zero mean value and variance given by $\sigma_r = (2D_S\Delta t)^{1/2}$. In our simulations, we model the particle-wall interactions via a shifted Yukawa-like potential:

$$\beta U(r) = \beta U(x) = \varepsilon\frac{e^{-\kappa x/a}}{(x-a)^2} \quad (5)$$

where x denotes the shortest distance between the particle's center and the inverse opal, as shown in the left panel of Figure 3, and $\beta = (k_B T)^{-1}$.

Let us briefly discuss the choice of the functional form and the values of the numerical parameters involved in the particle-wall interaction employed in eq 5 above. The main requirement for this potential is that it has to capture the effects of confinement. In this sense, and in the absence of any microscopic information on the form of the interaction, the simplest choice would have been the hard-wall potential, which would diverge at $x = a$ and vanish for all values $x > a$. However, such as choice is, on the one hand, impractical for BD because it would require the performance of costly, event-driven BD simulations and, on the other hand rather, unrealistic because it is expected that residual forces (dispersion, electrostatic, etc.) are indeed present between the tracer and the confining walls. At the
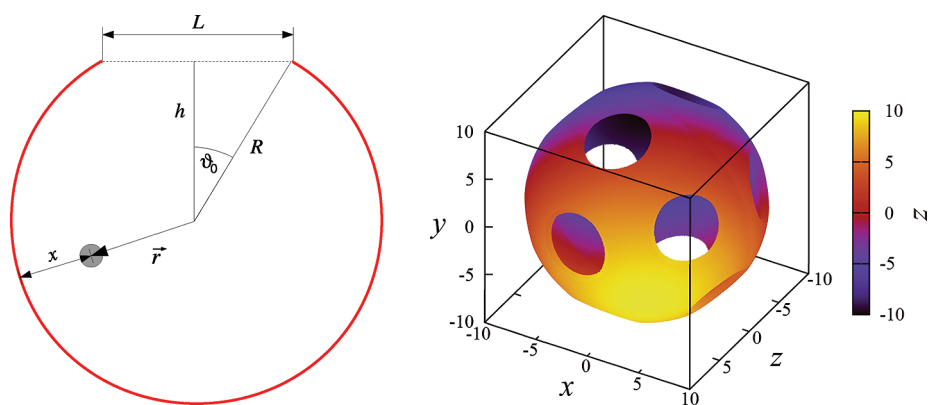
Figure 3. Schematic representation of a confining capped sphere with one opening (left) and actual inverse opal cavity employed in the simulations (right).

same time, we wish to keep the modeling as simple as possible. We therefore resort to capturing with the interaction potential only the salient, key characteristics, namely:

1. The divergence at $x = a$ which is guaranteed by the denominator, $(x - a)^2$, in eq 5.
2. A screened "electrostatic" nature, which is captured by the exponentially damped numerator, $e^{-\kappa x/a}$.
3. The independence of the interaction on the particle size a, which is guaranteed by eq 5 since, when the particle-wall distance x is expressed in units of a, the interaction takes a universal, a-independent form. In this way, we minimize the number of fit parameters, and the effects of confinement are all captured in the ratio a/R, which does not explicitly enter the form of the interaction for distances $x > a$.

There are two parameters that have to be fixed, the strength ε and the dimensionless inverse decay length κ. For the former, we choose a value $\varepsilon = 5$, which corresponds to interaction energies of the order $k_B T$ when the particle center lies a few particle radii away from the wall. On the other hand, κ is employed as the only fit parameter, under the assumption that the interaction becomes vanishingly small when x exceeds several particle radii. Comparison with experimental results (to follow) led us to fixing $\kappa = 0.35$, which corresponds to a decay length of about three particle radii, consistent with the underlying idea of putting focus onto confinement, as was mentioned above.

In our modeling, we have not taken hydrodynamic interactions (HI) *explicitly* into account and focused instead on a combination of overdamped dynamics with the effects of the confining cavities. Nevertheless, the influence of HI are *implicitly* included in the simulations through the fitting of κ. Indeed, the fact that $\beta U(r)$ decays over roughly three particle radii, which is typical for the HI between a sphere and plane, indicates that, additionally to the short-ranged steric and electrostatic interactions, hydrodynamics *does* play an important

role. However, this simplified approach is clearly justified in two distinct limits. For $a/R \ll 1$, the physical size of the particle is so small that explicit HI are indeed negligible. For $a \rightarrow L/2$, the dominant effect bringing about the delay in the particle diffusion is the bottleneck caused by the hindrance of the tracer to pass through the connecting pores between two spherical cavities of the inverse opal. To keep the modeling as simple as possible and to bring forward the effects of the confining walls, we have thus chosen not to model HI explicitly for all intermediate sizes of the tracer particle, as well. The remarkable agreement between experimental and simulation results offers *a posteriori* justification for our approximations. We emphasize that the *same* interaction and numerical parameters were used to model *all* experimental results.

We make use of the Einstein–Stokes equation to relate the short-time diffusion coefficient D_S to the drag coefficient $\xi = 6\pi\eta a$ (η being the viscosity of the solvent), which leads to the relation

$$D_S = \frac{k_B T}{\xi} \tag{6}$$

We verified the correct implementation of the algorithms by measuring the mean-square displacement of a free particle (vanishing deterministic force on the particle, $\mathbf{F}(r) = 0$), calculating the long-time diffusion coefficient D_{free} *via* the relation $\langle \Delta r^2(t) \rangle \equiv \langle [\mathbf{r}(t) - \mathbf{r}(0)]^2 \rangle = 6 D_{free} t$, and checking that $D_{free} = D_S$. In other words, for free particles, long- and short-time diffusion coefficients coincide.

The coincidence of the long- and short-time diffusion coefficients does not hold up anymore in the confined case. Instead, the long-time diffusion coefficient D strongly depends on the ratio L/R, which together with the number of openings per void (12 for our i-opals) determines the size of the permeable surface. In addition, the tracer-to-cavity size ratio, a/R, is expected to have a clear influence on diffusivity, as well, so that we end up with a long-time diffusion coefficient $D = D(L/R, a/L)$. This coefficient is highly

correlated to the escape probability, and we can distinguish between two extreme cases: if the penetrable area approaches the surface area of the void (that is, the theoretical limit in which no solid surface would exist anymore), then we would end up with $D = D_S$. The opposite extreme case would be an escape volume that is vanishingly small, that is, if there were no openings in the cavity. In such a situation, the diffusing particle would never be able to escape its confining volume. Additionally, the factor plays also a significant role concerning the diffusion process: first, it directly influences the short time diffusion coefficient in eq 6 and thus the velocity of the diffusing tracer; second, the larger a is chosen, the smaller one can consider the escape area to become at fixed L and R until it vanishes completely at $a = L/2$.

Following the present information from the experiments, we have chosen values of the particle radius belonging in the interval $a/R \in [0.01, 0.30]$, which approach the aforementioned case $a \rightarrow L/2$ at the upper limit. In order to analyze this transitional regime, we measured the mean escape time $\langle \tau_{esc} \rangle$ of the embedded particle from the cavity of the inverse opal, where the brackets $\langle ... \rangle$ denote an ensemble average over different realizations of the thermal fluctuations. The diffusion through the inverse opal can then be seen in a coarse-grained fashion in time, as a random walk on a lattice of step $\sim R$ and waiting time $\langle \tau_{esc} \rangle$ on each lattice site, leading to an expression for the long-time diffusion coefficient D, which is well-known from the theory of random walks, namely, $6D = R^2/\langle \tau_{esc} \rangle$.

In the case of a free particle of radius a, the expected escape time from a cavity of radius R can be written as $\langle \tau_{esc} \rangle = \tau_{free}$, where

$$\tau_{free} = \frac{R^2 \pi \eta a}{k_B T} \qquad (7)$$

Equation 7 immediately results in $D_{free} \sim a^{-1}$, as experimentally found for the tracer diffusivities in the free solution; note that the sphere of radius R in eq 7 is fictitious. Moreover, we define a time scale τ_0 that is independent of the particle size, and it corresponds to the time needed for a free particle of radius R to escape from a "cavity" of the same size, viz.

$$\tau_0 = \frac{R^3 \pi \eta}{k_B T} \qquad (8)$$

The advantage of setting τ_0 as the unit of time in our simulations is that we can directly compare the expectation values of the escape times $\langle \tau_{esc} \rangle$ for arbitrary combinations of the parameters a/L and L/R and immediately translate ratios of the same into the slowdown factor, which is the quantity measured in the experiments. Note also that, in this way, we can rewrite eq 7 as $\tau_{free} = a\tau_0/R$, which is exact for a free particle. To gain a feeling about orders of magnitude, we quote a typical value for a setup in which $R \approx 100$ nm in
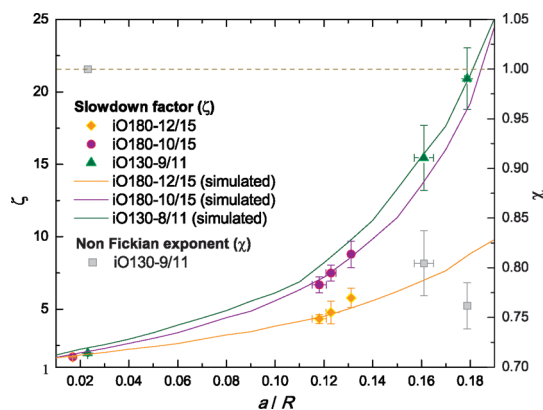

Figure 4. Slow-down factor ζ for the i-opals as a function of the reduced radius a/R: symbols denote experimental data; continuous lines are simulation data. The right vertical axis shows the value of the exponent χ in the time dependence of the tracer mean-square displacement.

aqueous solvent and at room temperature. Finally, we note that the above considerations hold only if the long-time motion of the particle is indeed diffusive, that is, if the mean-square displacement scales linearly with time, an assumption that will be shown to hold in what follows.

Comparison between Experiment and Simulation. The comparison between the experimental diffusion times is visualized in Figure 4 in the reduced plot of the slowdown factor ζ plotted against the ratio a/R, which is a measure of the confinement, and for the three different L/R values. The delay factor is calculated as $\zeta \equiv \langle \tau_{esc} \rangle / \tau_{free}$ in the BD simulations and $\zeta \equiv \tau$(in i-opals)/τ(in free solution) in the FCS experiment. The two main experimental findings are discussed in what follows.

First, even in the limiting case $a \ll R$, the value ζ_0 of the slow-down factor remains strictly larger than 1, implying that even in the ideal, point-particle case ($a/R \rightarrow 0$), a confined probe is slower than a free one. Though the strict case is problematic from a mathematical point of view, since the particle would formally experience vanishing friction with the solvent (see eq 6), the finding is physically intuitive: a free and a confined point particle needs the same time to reach diffusively a distance R, but whereas the free particle then immediately "escapes", the confined one will only do so if it happens to hit the cavity at the opening; otherwise, it will remain confined and will attempt to escape with subsequent diffusive motion. In this respect, we expect the quantity ζ_0 to become insensitive to the particle size and to depend mainly on the ratio L/R, albeit in some weak fashion. From the simulation, and if we were indeed in the limit in which the ratio a/R was so small as to be irrelevant, we would expect $\zeta \approx \zeta_0$ to drop monotonically with the ratio L/R, which is not yet the case for the smallest values, $a/R = 0.01$ considered there. Therefore, the particle size is still relevant, and so we can conclude by extrapolation that the limiting value ζ_0 should depend rather weakly on the
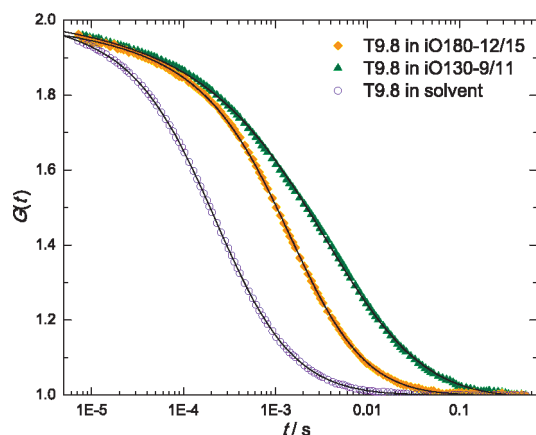
Figure 5. Experimental $G(t)$ for T9.8 in two confining i-opals as opposed to its diffusion in free solution. The solid lines denote the representation of $G(t)$ by eq 3 (in free solution and in iO180-12/15) and eq 9 (in iO130-9/11).

opening-to-cavity ratio L/R. In fact, the simulated $\zeta_0 = 1.7$ (iO180-12/15) and $\zeta_0 = 1.9$ (iO180-10/15) follow this anticipated trend.

These values capture well the experimental $\zeta_0 = 1.80 \pm 0.06$ for the smallest T1.3 tracer. In the case of the third i-opal (iO130-9/11), for which an anomalous diffusion is observed (see below), the simulations overestimate the experimental value by about 20% (Figure 4). This deviation, though still within fairly good limits of agreement, could easily be taken care of by employing slightly different parameters for the diffusant−wall interaction. However, for reasons of consistency and parsimony, we refrained from doing so in the modeling at hand. In this context, we note that the translational motion for all four tracers in i-opals with $a/R < 0.14$, realized with the same cavity radius $R = 75$ nm (Table 1), is well described by a normal Fickian diffusion as in the free solution. The simulated results for the structural characteristics of these two i-opals denoted by the continuous solid lines in Figure 4 provide a good description of experimental data. For stronger confinement realized with the iO130-9/11 i-opal, the experimental $G(t)$ for the QD deviates from a single Fickian diffusion which, however, nicely holds for the molecular T1.3 tracer. For this i-opal, $G(t)$ for the QDs can be best fitted by a single non-Fickian process[30] taking into account the blinking effect:

$$G(t) = 1 + (1 - Bt^{2-m})\frac{1}{N}\frac{1}{\left[1 + \left(\frac{t}{\tau}\right)^{\chi}\right]\sqrt{1 + \left(\frac{t}{\tau}\right)^{\chi}\frac{1}{S^2}}} \quad (9)$$

The exponent $\chi < 1$ denotes a subdiffusional behavior for the mean-square displacement, $\langle\Delta\mathbf{r}^2(t)\rangle \sim t^{\chi}$. This situation is illustrated in Figure 5 for the translational motion of T9.8 in free solution and in two i-opals. The shape of $G(t)$ is clearly broader for the motion of T9.8 in the stronger confining environment of iO130-9/11 with $a/R \approx 0.18$ than in iO180-10/15 and is well described by

eq 9 with $\chi < 1$; the values of χ are plotted in Figure 4. The deviation from the simple Fickian diffusion increases with a/R, and the dynamic frustration is manifested in the enhanced reduction of the particle diffusivity as seen in Figure 4. The simulations can capture this strong slowing down using the same particle-wall interactions but adjusting the geometrical confinement, that is, decreasing the ratio L/R by about 10% from 9/11 to 8/11. As a matter of fact, the simulations can also capture this strong slowing down at the experimentally assessed value of $L/R = 9/11$, but allowing for a stronger repulsion with the wall of T9.8 than for the other two i-opals.

The nature of the diffusive process is, as mentioned above, characterized by the exponent χ in $\langle\Delta\mathbf{r}^2(t)\rangle \sim t^{\chi}$, whereas $\chi = 1$ characterizes the usual Fickian diffusion, the cases $\chi < 1$ ($\chi > 1$) correspond to subdiffusive (superdiffusive) behavior.[31,32] The key in determining the value of the exponent χ above lies in the form of the probability distribution function $p(\tau_{esc})$ of the escape time τ_{esc} from a cavity of size R. Indeed, the total time t is the sum of a large number of independent and identically distributed random variables τ_{esc}, the asymptotic behavior of $p(\tau_{esc})$ for large values of its argument determines, then, the stable distribution of their sum. In particular, subdiffusive behavior will result if $p(\tau_{esc})$ has a power-law tail of the form[33,34]

$$p(\tau_{esc}) = \frac{t_0^{\alpha}}{\tau_{esc}^{1-\alpha}} \quad (10)$$

with an arbitrary time constant t_0 and $\alpha \in (0,1)$. On the contrary, any probability distribution that decays to zero faster than that of eq 10 above as $\tau_{esc} \rightarrow \infty$ will lead to normal diffusion (i.e., $\chi = 1$).

Computer simulations offer the possibility to measure the probability distribution $p(\tau_{esc})$ by performing statistics on the escape time from the cavity. We have done so for all parameter combinations studied in our system, and we show representative results in Figure 6. As can be seen there, the distribution is exponentially decaying and can be very well fitted with the functional form

$$p(\tau_{esc}) = \frac{1}{\tau_c}\exp\left(-\frac{\tau_{esc}}{\tau_c}\right) \quad (11)$$

with a characteristic time constant τ_c that depends on the parameters L/R and a/L and thus sets the characteristic escape time from the cavity. This form can be understood when the escape processes are considered as a sequence of independent yes/no (i.e., escape/no escape) random trials, each of which yields success with probability p^*. Due to the high symmetry of our system, the probability p^* is approximately proportional to the ratio between the penetrable area and the surface area of the void. Hence, p^* becomes very small as $a \rightarrow L/2$, and the diffusion through the i-opals can be regarded as a Poisson process, reflected in the form of 11eq 11.

In Table 2, we summarize the results for three representative systems, and we show in particular the
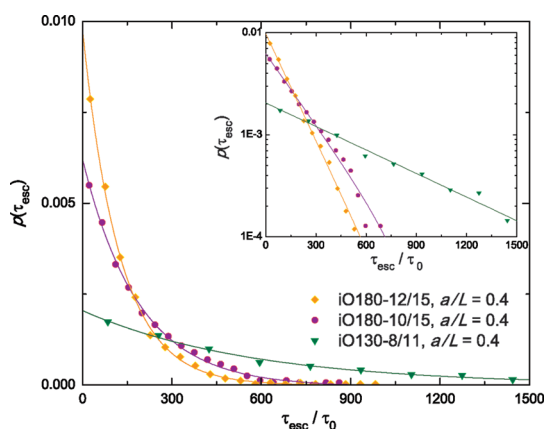
Figure 6. Probability distribution $p(\tau_{esc})$ of the escape times τ_{esc} as obtained in the Brownian dynamics simulations for three different combinations of system parameter (points). Also shown are the fits by decaying, single exponentials, eq 11 (lines). Inset: semilogarithmic plot, emphasizing the quality of the fit for large values of the abscissa.

numerical values obtained for the expectation value of the escape time, $\langle\tau_{esc}\rangle$, obtained directly from the simulations and for the time constant, τ_c, obtained from the representation of the data by eq 11, to an exponential; due to uncertainties in the numerical experiment, both quantities carry error bars. For a random variable τ_{esc} following the distribution of eq 11, the equality $\langle\tau_{esc}\rangle = \tau_c$ should hold. A comparison between the values in the second and third columns of Table 2 shows that, within error bars, this equality is indeed well-satisfied. There is thus overwhelming evidence from simulation that the distribution of escape times is indeed decaying to zero much faster than the family of distributions of eq 10 (which imply $\chi < 1$), and thus the diffusion process in the regular periodic i-opal should be normal Fickian diffusion with an exponent $\chi = 1$.

Though this is in agreement with experiment for all other cases of tracer particles and confining structures, there is a discrepancy with the observed anomalous diffusion experiment for the most confined case of QDs in the iO130-9/11 i-opal. We believe that the subdiffusive exponent measured in the experiments for the last case is only an apparent one and that the process is strictly diffusive. The reason for the appearance of an exponent $\chi < 1$ (which, in addition, seems also to depend on the tracer size) probably lies in the presence of at least two simultaneous diffusion processes, a faster and a slower one, caused by inevitable polydispersity in the opening size L. Indeed, as long as the particle radius is much smaller than the opening, through which escape from the cavity takes place, polydispersity should not have any measurable effect. However, as the limit $a \rightarrow L/2$ is approached from below, any polydispersity in the opening size can have drastic effects because the escape time grows very fast (see Figure 4) and eventually diverges at $a = L/2$. Tight confinement and tracer-wall interactions realized in mesoporous silica channel systems render the

TABLE 2. Waiting Times for a Confined Tracer Particle[a]

i-opals and tracer particles	$\langle\tau_{esc}\rangle/\tau_0$	τ_c/τ_0
iO130-8/11, $a/L = 0.4$	573.2 ± 32.9	568.4 ± 20.7
iO180-10/15, $a/L = 0.4$	182.3 ± 9.0	188.0 ± 5.3
iO180-12/15, $a/L = 0.4$	130.2 ± 7.6	124.6 ± 2.4

[a] The first column shows the characteristic parameters of the i-opal (physical system), the second the expectation value of the escape time τ_{esc} as obtained from the simulation, and the third the value of the corresponding time constant τ_c, obtained by fitting the distribution $p(\tau_{esc})$ with an exponential, eq 11 of the main text.

structure of the molecule trajectories very heterogeneous as was recently revealed by wide-field fluorescence microscopy.[2] The assumption, therefore, of the existence of two subprocesses, a fast and a slow one, caused by polydispersity, which gives rise to an apparent subdiffusive behavior at intermediate times, is supported by the fact that the phenomenon becomes visible only for large values of the tracer size. Evidently, normal diffusion should settle in at sufficiently long observation times. An alternative explanation would be the existence of attractive patches ("trapping sites") within the cavities of the i-opal, in which tracer particles occasionally reside for long times. However, such an effect should also be visible in the diffusive behavior for small radii, which is not the case. Therefore, the polydispersity scenario is the most realistic assumption for the explanation of the apparent $\chi < 1$ exponent.

CONCLUSIONS

Periodic porous nanostructures are excellent platforms for the study of particle diffusion under controlled confinement conditions. Three relevant scales—particle radius a, hole diameter L, and cavity radius R (see Figure 3)—along with particle-wall interactions can be tuned. In this work, we have first examined the diffusion law and the particle diffusion slowing down as a function of a/R at the confining environment of three i-opals characterized by the ratio L/R while keeping the same particle-wall interaction potential. Brownian dynamics simulations predicted a normal Fickian diffusion for all examined particles and i-opals with different geometrical confinements. The translational diffusion dropped almost exponentially with the "frustration ratio" a/R at a constant confinement environment L/R. Relaxing the geometrical constraint (increase of L/R) the slow-down was reduced due to the increasing particle escape rate from the cavity through the opening, L. At vanishing $a/R \rightarrow 0$, there was a residual slowing down ($\zeta_0 \sim 1.8$) as the particle remained confined when $L/R < 1$. The predicted confined dynamics in i-opals was confirmed by the present experiment. Only for the strongest confining medium (lowest L/R) and highly frustrated particle (large a/R) an anomalous diffusion was observed. Under these severe conditions, the low but finite size polydispersity can impact the diffusion mechanism.
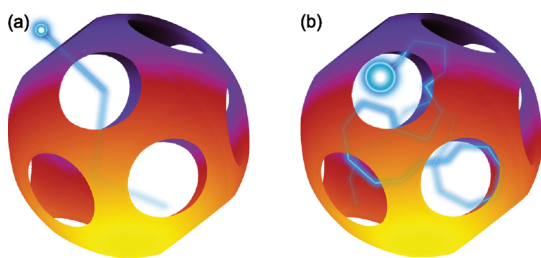
Figure 7. Sketch of the process of multiple collisions that a tracer particle undergoes against the cavity walls before it escapes to the neighboring cavity. For small ratios a/L between particle size and cavity openings (a), a small number of bounces suffices, but for large ones (b), a large number of collisions with the walls takes place before the particle escapes.

The theoretical modeling and simulation revealed that the long-time motion of the tracer particles in this highly ordered, porous nanostructure is strictly diffusive. In particular, the diffusion of the quantum dots can be visualized as a succession of "bounces" against the cavity walls, which delay the escape from the interior of the same, until a successful event takes place in the cavity and the particle translocates to the interior of the adjacent one. There, the process repeats itself, and a random walk with a characteristic step length R and characteristic time τ_{esc} results. Thus, the "bouncing-and-escape" succession within a cavity is the mechanism responsible for the overall, measured and calculated, delay factors. Naturally, the number of bouncing events preceding escape grows as the ratio a/L increases, a fact that is schematically depicted in Figure 7.

This work is the first clear step toward a systematic elucidation of the key parameters of diffusion in continuous porous networks, namely, probe size (a), connecting pores (L), and confining void (R). Variation of the particle asphericity (from spheres to rods) and tuning of the interactions (charged particles, soft interfacing of the walls) are two examples in the rich parameter space to be still explored. Yet, diffusion is ubiquitous in diverse systems and plays a pivotal role in cellular mass transport. Identification, characterization, and design of the diffusion mechanisms can have important technical and scientific ramifications on separation techniques, drug delivery, cellular transport, and energy storage in microfluidic systems, spongy matter, and hierarchically structured materials. A detailed understanding of the confinement and interaction effects is a precondition to access fundamental concepts such as mass transport management in such interconnected porous networks. Further, specifically targeted membranes and porous system can, in the light of our modeling, be engineered and tailored for specific real-world uses with great predictive ease and finely tuned properties.

METHODS

Materials. One molecular dye (Alexa647) and three quantum dots (QD-X) with spherical shape and different sizes were purchased from Invitrogen. Their hydrodynamic radii were measured by fluorescence correlation spectroscopy (FCS) in ultradilute (nM) aqueous solutions at ambient temperature. The structural characteristics of the molecular (T1.3) and particle-like (T8.8, T9.2 and T9.8) probes are listed in Table 3.

Preparation of the Inverse Opals. Inverse colloidal crystals (i-opals) were prepared[35] by co-deposition of monodisperse colloidal polystyrene (PS) and silica (SiO$_2$) nanoparticles (LUDOX SM, Sigma Aldrich) on plasma-treated glass slides (150 μm thickness). We used PS particles with a diameter of 180 and 130 nm in aqueous suspension at a concentration of 1 wt %, and the concentration of the silica nanoparticles (radius 7 nm) was adjusted to be 0.3 wt %. Vertical lifting deposition (VLD) was conducted at 20 °C, 50% RH at a lifting speed of 400 nm/s. We deposited the samples on plasma-treated glass slides (150 μm thickness). After VLD, the PS particles were removed by calcination for a few hours in a tube oven at 450 °C in air (heating rate ~10 K/min). Three different i-opals were fabricated (Table 1) for the purpose of the present study: one (iO130-9/11) with nominal cavity diameter of 130 nm and two with 180 nm using different methods (co-deposition and SolGel) for SiO$_2$ nanoparticle infiltration into the PS colloidal crystals (iO180-12/15 and iO180-10/15, respectively). Intentionally, we designed the systems iO180-12/15 and iO130-9/11 to provide periodic structures for diffusion through comparable holes but different cavity sizes. Conversely, the samples iO180-12/15 and iO180-10/15 i-opals allow for the study of diffusion in confining periodic structures with the same voids but different hole sizes; the latter sample was prepared by filling the interstitial spaces between the PS particles with SolGel prior to calcination. The SolGel filling led to a reduction of the pore diameter in the iO180-10/15 sample. The i-opal structures were characterized by SEM on a LEO Gemini 1530 microscope (Carl Zeiss AG, Oberkochen, Germany) with acceleration voltage of 1 kV in secondary electrons InLens detection mode. We obtained the actual cavity radius R and the hole diameter L from the SEM images as seen in Figure 8a for iO130-9/11 system. As seen in this figure, cracks exist between blocks of ordered structure. These can be categorized in large cracks between monoliths of i-opals and smaller internal cracks including point and line defects. Whereas the micrometer sized cracks between monoliths can be assessed by SEM, smaller cracks in the interior of an i-opal cannot be characterized directly.

Fluorescence Correlation Spectroscopy. All measurements were performed on a commercial FCS setup[36] (Carl Zeiss, Jena, Germany) consisting of the module, ConfoCor 2, and an inverted microscope, Axiovert 200 model. A 40× Plan Neofluar objective (numerical aperture 1.2; working distance 0.29 mm) and ultrapure water (filtered through a Milli-Q purifaction system, resistivity 18.2 MOhm × cm) as immersion liquid were used. The FCS experiment was concurrently performed with two tracers using excitation at 488 and 633 nm. The emission was collected after splitting the signal by means of a NFT635 dichroic mirror and filtering with a long-pass LP655 filter for the fluorescence light from the λ = 633 nm excitation (channel 1) and with a band-pass filter (BP560-615) for the fluorescence light at λ = 488 nm excitation (channel 2). Avalanche photodiodes capable of single-photon counting were used for detection. Reusable Attofluor chambers were employed for the measurements. All experiments were conducted at 21 ± 1 °C.

Prior to observation, the samples were rinsed with ethanol, dried at room temperature, and mounted in the Attofluor chambers. Then, we added 600 μL of HEPES buffer, followed by 150 μL of T1.3 and 150 μL of the QD, both at 120 nM, in order to achieve comparable concentration for both tracers. It took about 30 min to reach constant fluorescence signal from a homogeneous system. The time-dependent fluctuations of the

TABLE 3. Size and Surface Characteristics of the Fluorescent Particles

tracers	Alexa647	QD525	QD545	QD585
code	T1.3	T8.8	T9.2	T9.8
R_h (nm)	1.3	8.8	9.2	9.8
core	molecular dye	CdSe	CdSe	CdSe
shell	N/A	ZnS	ZnS	ZnS
coating	N/A	amphiphilic polymer (unspecified)	amphiphilic polymer (unspecified)	amphiphilic polymer (unspecified)
surface modification	N/A	carboxylic groups (c/a 100)	carboxylic groups (c/a 100)	carboxylic groups (c/a 100)
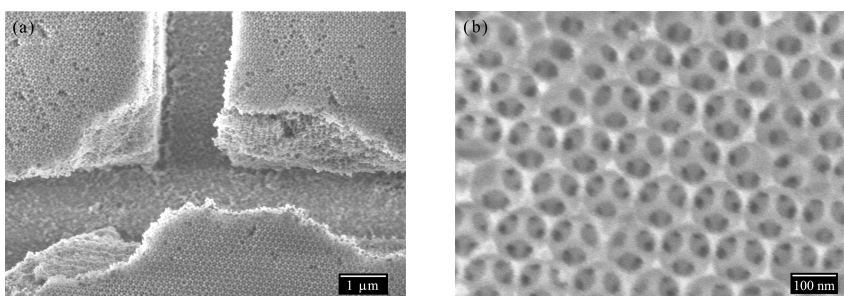
Figure 8. Overview (a) and high-magnification (b) SEM images for SEM of iO130-9/11.

fluorescent intensity $\delta I(t)$ were recorded and analyzed by an autocorrelation function $G(t) = 1 + \langle \delta I(t')\delta I(t'+t)\rangle/\langle I(t')\rangle^2$. The accumulation time was varied from about 3 min, for diffusion in free solutions, and up to about 10 min, for diffusion in the i-opals. The necessary total accumulation duration was subdivided in 30 s intervals in order to enable removal of occasionally spurious signals due to aggregates.

The big cracks mentioned in the previous section regarding the SEM images of Figure 8 had no effect on the FCS experiment since they were much larger than the focal volume and could be easily recognized and hence avoided. The small internal cracks with typical size ranging from a cavity length scale (completely open cage) up to the observation volume would have caused detectable signal disturbances and would have been detected by scanning different regions in the films. All recorded autocorrelation functions, which had been systematically verified, represent structurally coherent regions at least over the lateral dimension (~300 nm) of the observation volume. Furthermore, autocorrelation functions from various spots within the monolithic i-opal regions featured identical decay curves, which exemplifies the homogeneity of the internal i-opal structure.

REFERENCES AND NOTES

1. Yang, S. Y.; Yang, J.-A.; Kim, E.-S.; Jeon, G.; Oh, E. J.; Choi, K. Y.; Hahn, S. K.; Kim, J. K. Single-File Diffusion of Protein Drugs through Cylindrical Nanochannels. *ACS Nano* **2010**, *4*, 3817–3822.
2. Lebold, T.; Jung, C.; Michaelis, J.; Bräuchle, C. Nanostructured Silica Materials as Drug-Delivery Systems for Doxorubicin: Single Molecule and Cellular Studies. *Nano Lett.* **2009**, *9*, 2877.
3. Shao, Z.; Haile, S. A High-Performance Cathode for the Next Generation of Solid Oxide Fuel Cells. *Nature* **2004**, *431*, 170–173.
4. Jackson, E. A.; Hillmyer, M. A. Nanoporous Membranes Derived from Block Copolymers: From Drug Delivery to Water Filtration. *ACS Nano* **2010**, *4*, 3548–3553.
5. Volkmuth, W. D.; Austin, R. H. DNA Electrophoresis in Microlithographic Arrays. *Nature* **1992**, *358*, 600–602.
6. Han, J.; Craighead, H. G. Separation of long DNA Molecules in a Microfabricated Entropic Trap Array. *Science* **2000**, *288*, 1026–1029.
7. Fakhri, N.; MacKintosh, F. C.; Lounis, B.; Cognet, L.; Pasquali, M. Brownian Motion of Stiff Filaments in a Crowded Environment. *Science* **2010**, *330*, 1804–1807.
8. Wei, Q.; Bechinger, C.; Leiderer, P. Single-File Diffusion of Colloids in One-Dimensional Channels. *Science* **2000**, *287*, 625–627.
9. Wang, B.; Anthony, S. M.; Bae, S. C.; Granick, S. Anomalous yet Brownian. *Proc. Natl. Acad. Sci. U.S.A.* **2009**, *106*, 15160–15164.
10. Nykypanchuk, D.; Strey, H. H.; Hoagland, D. A. Brownian Motion of DNA Confined within a Two-Dimensional Array. *Science* **2002**, *297*, 987–990.
11. Park, S.; Park, I.; Chang, T.; Ryu, C. Y. Interaction-Controlled HPLC for Block Copolymer Analysis and Separation. *J. Am. Chem. Soc.* **2004**, *126*, 8906–8907.
12. Striemer, C. C.; Gaborski, T. R.; McGrath, J. L.; Fauchet, P. Charge- and Size-Based Separation of Macromolecules Using Ultrathin Silicon Membranes. *Nature* **2007**, *445*, 749–753.
13. Retan, N. K.; Juthajan, A.; Lindmo, T.; de Lange Davies, C. Macromolecular Diffusion in the Extracellular Matrix Measured by Fluorescence Correlation Spectroscopy. *J. Biomed. Opt.* **2008**, *13*, 054040.
14. Nikoubashman, A.; Likos, C. N. Flow-Induced Polymer Translocation through Narrow and Patterned Channels. *J. Chem. Phys.* **2010**, *133*, 074901.
15. Doi, M.; Edwards, S. F. *The Theory of Polymer Dynamics*; Oxford University Press: New York, 1999.
16. Cherdhirankorn, T.; Harmandaris, V.; Juhari, A.; Voudouris, P.; Fytas, G.; Kremer, K.; Koynov, K. Fluorescence Correlation Spectroscopy Study of Molecular Probe Diffusion in Polymer Melts. *Macromolecules* **2009**, *42*, 4858–4866.
17. Fu, Y.; Ye, F.; Sanders, W. G.; Collinson, M. M.; Higgins, D. A. Single Molecule Spectroscopy Studies of Diffusion in Mesoporous Silica Thin Films. *J. Phys. Chem. B* **2006**, *110*, 9164–9170.
18. Kirstein, J.; Platschek, B.; Jung, C.; Brown, R.; Bein, T.; Bräuchle, C. Exploration of Nanostructured Channel Systems by Single Molecule Probes. *Nat. Mater.* **2007**, *6*, 303.
19. Rigler, R.; Elson, E. S. *Fluorescence Correlation Spectroscopy*; Springer: Berlin, 2001.

20. Haustein, E.; Schwille, P. Ultrasensitive Investigations of Biological Systems by Fluorescence Correlation. *Methods* **2003**, *29*, 153–166.

21. Lumma, D.; Keller, S.; Vilgis, T.; Radler, J. O. Dynamics of Large Semiflexible Chains Probed by Fluorescence Correlation Spectroscopy. *Phys. Rev. Lett.* **2003**, *90*, 218301.

22. Zhao, J.; Granick, S. How Polymer Surface Diffusion Depends on Surface Coverage. *Macromolecules* **2007**, *40*, 1243–1247.

23. Hohlbein, J.; Steinhart, M.; Schiene-Fischer, C.; Benda, A.; Hof, M.; Hubner, C. G. Confined Diffusion in Ordered Nanoporous Alumina Membranes. *Small* **2007**, *3*, 380–385.

24. Sato, A.; Pennec, Y.; Shingne, N.; Albrecht-Thum, T.; Knoll, W.; Steinhart, M.; Djafari-Rouhani, B.; Fytas, G. Tuning and Switching the Hypersonic Phononic Properties of Elastic Impedance Contrast Nanocomposites. *ACS Nano* **2010**, *4*, 3471–3481.

25. Cherdhirankorn, T.; Retsch, M.; Jonas, U.; Butt, H. J.; Koynov, K. Tracer Diffusion in Silica Inverse Opals. *Langmuir* **2010**, *26*, 10141–10146.

26. Stefani, F. D.; Hoogenboom, J. P.; Barkai, E. Beyond Quantum Jumps: Blinking Nanoscale Light Emitters. *Phys. Today* **2009**, *62*, 34–39.

27. Bachir, A. I.; Kolin, D. L.; Heinze, K. G.; Hebert, B.; Wiseman, P. W. A Guide to Accurate Measurement of Diffusion Using Fluorescence Correlation Techniques with Blinking Quantum Dot Nanoparticle Labels. *J. Chem. Phys.* **2008**, *128*, 225105.

28. Enderlein, J.; Gregor, I.; Patra, D.; Fitter, J. Art and Artefacts of Fluorescence Correlation Spectroscopy. *Curr. Pharm. Biotechnol.* **2004**, *5*, 155–161.

29. Wang, J.; Li, Q.; Knoll, W.; Jonas, U. Preparation of Multilayered Trimodal Colloid Crystals and Binary Inverse Opals. *J. Am. Chem. Soc.* **2006**, *128*, 15606–15607.

30. Fatin-Rouge, N.; Starchev, K.; Buffle, J. Size Effects on Diffusion Processes within Agarose Gels. *Biophys. J.* **2004**, *86*, 2710–2719.

31. Wong, I. Y.; Gardel, M. L.; Reichman, M. L.; Weeks, E.; Valentine, M. T.; Bausch, A.; Weitz, D. A. Anomalous Diffusion Probes Microstructure Dynamics of Entangled F-Actin Networks. *Phys. Rev. Lett.* **2004**, *92*, 178101.

32. Saxton, M. J. A Biological Interpretation of Transient Anomalous Subdiffusion. I. Qualitative Model. *Biophys. J.* **2007**, *92*, 1178–1191.

33. Bouchaud, J.-P.; Georges, A. Anomalous Diffusion in Disordered Media: Statistical Mechanisms, Models and Physical Applications. *Phys. Rep.* **1990**, *195*, 127–293.

34. Paul, W.; Baschnagel, J. *Stochastic Processes. From Physics to Finance*; Springer: Berlin, 1999.

35. Li, Q.; Retsch, M.; Wang, J. J.; Knoll, W. G.; Jonas, U. Porous Networks through Colloidal Templates. *Top. Curr. Chem.* **2009**, *287*, 135–180.

36. Cherdhirankorn, T.; Koynov, K.; Peneva, K.; Muellen, K.; Fytas, G. Fluorescence Correlation Spectroscopy Studies of Tracer Diffusion in Polystyrene Solutions. *J. Phys. Chem. B* **2009**, *113*, 3355–3359.